

**Title:** A computational hemodynamics analysis on the correlation between energy loss and clinical outcomes for flow diverters treatment of intracranial aneurysm

**Running Title:** Energy Loss of Intracranial Aneurysms

**Authors:**

- **Corresponding author :** Tin Lok, CHIU is with Department of Mechanical Engineering, University of Hong Kong, Pokfulam, Hong Kong (e-mail: [u3003609@connect.hku.hk](mailto:u3003609@connect.hku.hk)). Phone number: +(852) 3917 2635, Fax number: +(852) 2858 5415. ORCID ID 0000-0002-2319-5168
- Abraham Yik Sau, TANG is with Department of Mechanical Engineering, University of Hong Kong, Pokfulam, Hong Kong (e-mail: [aystang@hku.hk](mailto:aystang@hku.hk)). ORCID ID XXX
- Anderson Chun On, TSANG is with Department of Surgery, Li Ka Shing Faculty of Medicine, University of Hong Kong, Pokfulam, Hong Kong (e-mail: [acotsang@hku.hk](mailto:acotsang@hku.hk)). ORCID ID XXX
- Gilberto Ka Kit, LEUNG is with Department of Surgery, Li Ka Shing Faculty of Medicine, University of Hong Kong, Pokfulam, Hong Kong (e-mail: [gilberto@hku.hk](mailto:gilberto@hku.hk)). ORCID ID XXX
- Kwok Wing, CHOW is with Department of Mechanical Engineering, University of Hong Kong, Pokfulam, Hong Kong (e-mail: [kwchow@hku.hk](mailto:kwchow@hku.hk)). ORCID ID XXX

**Title:** A computational hemodynamics analysis on the correlation between energy loss and clinical outcomes for flow diverters treatment of intracranial aneurysm

## **Abstract:**

Rupture of intracranial aneurysms might lead to permanent disability or even death. One possible endovascular treatment is to deploy flow diverters (FDs), reducing flow into the sac and promoting thrombosis. Computational fluid dynamics simulations were used to assess the flow patterns and dynamics. The concept of energy loss, as a measure of work done necessary to overcome flow resistance, will be utilized to correlate with clinical outcome. If a surgical operation is successful, the flow is diverted to a shorter path and energy loss should be reduced. Conversely, persistent flow in the sac associated with treatment failure will display increased energy loss, as blood is then squeezed through the stent pores. Four illustrative clinical cases, involving both bifurcation and sidewall aneurysms, were selected. To reduce the numerical complexity, earlier works in the literature had employed a porous medium approximation for the FDs. Here the FD was simulated explicitly as a virtual (or computer generated) stent which would likely provide a more accurate description. Furthermore, quantitative comparisons between the approaches of virtual stent and porous medium with typical parameters were conducted by examining the effective flow influx into the aneurysm.

## **1. Introduction**

An intracranial aneurysm (IA) is an abnormal swelling on the cerebral arteries. Prevalence of IA is approximately 3.2% of a population with a mean age of 50 [1]. Ruptured IAs would lead to intracranial hemorrhage and a significant mortality rate [2].

Despite the availability of endosaccular embolization in the clinical management of IAs, a few classes of aneurysms remain difficult to treat, typical examples being wide-neck [3] and large/giant aneurysms [4, 5]. An approach of endovascular treatments of IAs involves placing flow diverters (FDs) at the orifice of the aneurysm. FDs are mesh-like stents which can impede the blood flow into the aneurysmal sac, thus promoting thrombosis and occlusion. Even though the influx into the aneurysm is reduced, FD preserves the blood flow in the parent artery and side branches. The two types of FDs with most clinical data in the literature are the Pipeline Embolization Device [6, 7] (PED; Covidien Vascular Therapies, Mansfield, MA, USA) and Silk stent [8] (Balt, Montmorency, France). Different FD configurations will have an observable effect on the hemodynamics [9]. In this paper, the focus will be placed on PED. It consists of 48 strands fabricated from special alloys of cobalt-chromium and platinum-tungsten in a ratio of 3:1. A coverage of 35% is achieved [10], implying a porosity of 65% in terms of surface area available for fluid flow. The strands have an average diameter of 30  $\mu\text{m}$  according to the specifications from the manufacturer.

The treatment outcomes of FDs from clinical trials over the years are promising. A complete occlusion rate is observed for 76% of the patients at 6 months after surgical intervention [11]. However, there is still a non-negligible post treatment complication rate. The procedure-related permanent morbidity rate is 5% and the procedure-related mortality rate is 4% [11]. Hemodynamic flow patterns inside the aneurysm and along parent arteries [12] provide important information concerning the growth, rupture risks and prediction of clinical outcome [2, 13-15], and hence have been studied intensively. Numerical simulations of the blood flow patterns inside the circulation system employing Computational Fluid Dynamics (CFD) has

been widely used [16]. Aneurysm hemodynamics and post-treatment conditions have been simulated and studied [17-21]. CFD has indeed been employed extensively in previous studies on IAs deployed with FDs [18-24]. Several flow parameters have been introduced to correlate the underlying hemodynamics and the risk associated with aneurysm ruptures. They would be of great relevance in predicting the chance of success for FDs deployment as well. These parameters include energy loss (EL) [15, 22, 25], volume flow rate into aneurysm, wall shear stress [20, 23, 24] and have been investigated intensively.

In particular, energy loss [25] has gained attention in recent analysis on aneurysm hemodynamics. The idea is to compute the energy loss due to the blood flow between a point downstream and another point upstream of the aneurysm, both before and after surgical intervention. As the flow rates into the aneurysmal sac will be altered due to the deployment of FDs, this change of energy loss can be employed to assess aneurysm rupture risk and the likely outcome of the operation. This concept was examined in a recent study through evaluation of energy loss for 50 side-wall aneurysms and 50 bifurcation aneurysms model [15]. A trend of higher energy loss was observed in the data set of ruptured cases.

Another line of investigation has focused on the precise locations of the aneurysms, using as specific examples the Anterior Communicating Artery (AComA) [26] and the paraclinoid segment of the internal carotid artery [27]. Generally, energy loss was found to be higher in ruptured aneurysms in comparison with unruptured aneurysms. Besides rupture risk analysis, energy loss was correlated with different morphologic parameters [28, 29]. In simulations on bifurcation aneurysms [28, 30], angle configuration, ratio of daughter vessel diameter, aspect ratio and size ratio were correlated with energy loss. These works highlighted the importance of energy loss on aneurysm rupture and correlations with aneurysm geometry.

However, the change in energy loss after FD deployment has not been fully investigated. A previous study [22] attempted to correlate the concept of energy loss and the treatment outcome of FD deployment. A larger reduction in energy loss after the surgical operation usually indicated a clinically favorable outcome of aneurysm occlusion. In the numerical setting of that work, FDs were modeled as a porous medium, a domain which displayed a specific form of flow resistance. Computationally, there was an additional momentum sink term in the equations of motion with appropriate parameters.

The objective of our study was to investigate the effect of FDs on energy loss and other hemodynamic parameters by modeling the stent directly as a metallic mesh [21], with a patient-specific geometry and stent porosity similar to those in an actual clinical setting. Moreover, the relations between hemodynamic parameters and the two different modeling techniques, namely virtual stent and porous medium, were investigated.

## 2. Materials and Methods

### 2.1) Patients and Imaging data

Four patients with intracranial aneurysms at a tertiary referral neurosurgery center were selected for this study. They all went through FD treatment, and imaging data by angiograms were obtained 6 months later. Patients 1 and 2 were clinically successful cases. Patient 3 and 4 were clinically failed cases. The geometries of the aneurysms were sketched in Fig. 1. A successful case was defined here as achieving complete occlusion in the aneurysm 6 months after deployment of FDs, otherwise the surgical procedure will be termed a failed case. Patient data are tabulated in Table 1.

The study is approved by the Institutional Review Board of the hospital. No identifying information was used in this study. Only patient imaging data were used to reconstruct vessel model for simulations.

### 2.2) Geometrical model

Vessel geometries were reconstructed from pre-operation Magnetic Resonance Imaging (MRI) or Computer Tomography Angiography (CTA). After acquiring the CTA or MRI images, signal levels in voxels were displayed and vessel geometries were delineated by employing the software Mimics (Materialise, Leuven, Belgium), which converted DICOM imaging data to a 3D geometry in STL format. The computer-aided design software SOLIDWORKS 2012 (Dassault Systèmes SolidWorks Corp., Concorde, MA, USA) was then employed to achieve improved geometric configurations appropriate for CFD simulations. For each aneurysm geometry, a virtual stent was deployed to simulate the condition after the endovascular treatment. The stent porosities for each patient were tabulated in Table 1. Stent porosity was defined as the ratio of uncovered area of the neck orifice to the total area of the neck orifice. These porosities were determined according to the deployed stent diameter and the parent vessel diameter [7].

Pipeline flow diverter formed a periodic array of rhombus shaped patterns after the stent was deployed in the vessel (Fig. 2) [7]. There were two parameters affecting the porosity, the pitch,  $\theta$ , and the cell length,  $a$ . The cell length remained essentially constant and the strand width was known from the specification by the manufacturer, namely, 30  $\mu\text{m}$  in diameter. After determining the porosity, the pitch could be calculated retrospectively from the uncovered area.

In assessing the comparisons of the pre-operation and post-operation hemodynamic conditions, eight geometries were simulated, one pre-operation case without stent deployment and one post-operation case with FD for each patient geometry. This present research effort does *not* focus on comparing parameters across different patients, but instead we concentrate on assessing the change in parameters for the *same* patient. Stents were assumed to be rigid and non-elastic. Only those parts of the stent which were covering the aneurysm orifice or side vessel branch were modeled to save computational cost.

Tetrahedral elements were used and mesh sizes of 0.3 mm were chosen to maintain sufficient resolution. Locally refined grid was used when finer resolution was essential, for instance, 0.03 mm. The total number of elements used for each geometry is tabulated in Table 1. Mesh independence test was implemented on similar geometries in a previous study [21]. The size of the elements used was regarded as sufficient in resolution to provide accurate results. All meshes were generated by using GAMBIT 2.4.6 (ANSYS, Canonsburg, Pennsylvania, US).

A rigorous analysis on the geometrical effect of a virtual stent is worthwhile. Virtual stent has been studied in some previous works [21, 31]. Hence, the focus of our attention would be on the effect of porous medium. Besides the pre-operations and post-operations with a virtual stent implanted for two patients, stents were approximated as a porous medium, i.e. modeling the medium as a thin membrane with a known pressure drop characteristics. This membrane was assumed to be uniform and isotropic with a constant thickness. A pressure drop term, Eq. (1), was added in the momentum equation, and consists of a combination of the Darcy's Law and an additional inertial loss term:

$$\Delta p = -\left(\frac{\mu}{\alpha} v + C \frac{1}{2} \rho v^2\right) \Delta s \quad (1)$$

where  $\Delta p$  = pressure drop (Pa),  $\mu$  = dynamic viscosity ( $\text{kg m}^{-1} \text{s}^{-1}$ ),  $\alpha$  = permeability of the medium ( $\text{m}^2$ ),  $v$  = the velocity normal to the porous face ( $\text{m s}^{-1}$ ),  $C$  = pressure-jump coefficient ( $\text{m}^{-1}$ ),  $\rho$  = fluid density ( $\text{kg m}^{-3}$ ),  $\Delta s$  = thickness of the medium (m). Figure 3 gave an illustration of the porous medium modeling.  $\alpha$  and  $C$  were taken from works in the literature [32] based on simulations with SILK stents. There were two sets of parameters commonly used, depending on the orientation of FDs. They were termed '*tangential orientation*' and '*normal orientation*' in this paper, and numerical values are shown in Table 2. Both of them were used in the simulations and results were assessed.  $\Delta s$  was taken as 0.1 mm [22]. All patients showed a same qualitative trend on hemodynamics. Hence, the focus would be on Patients 1 & 3 to highlight the distinction between bifurcation and sidewall aneurysm. Eq. (1) is used only for the porous medium simulations of Patients 1 & 3 and is not used in the virtual stent simulations.

### 2.3) Fluid mechanics and boundary conditions

CFD simulations were performed on a commercial software package, FLUENT 6.3.26 (ANSYS, Canonsburg, Pennsylvania, USA). The underlying principles are mass conservation and momentum balance, governed by the continuity, Eq. (2), and Navier-Stokes equations, Eq. (3), respectively [33]:

$$\frac{\partial u_i}{\partial x_i} = 0, \quad (2)$$

$$\frac{\partial u_i}{\partial t} + u_j \frac{\partial u_i}{\partial x_j} = -\frac{1}{\rho} \frac{\partial p}{\partial x_i} + \frac{\mu}{\rho} \frac{\partial^2 u_i}{\partial x_j \partial x_j} \quad (3)$$

where  $u_i$  ( $i = 1, 2, 3$ ) are the components of velocity ( $\text{m s}^{-1}$ ),  $x_i$  ( $i = 1, 2, 3$ ) are the Cartesian spatial coordinates (m),  $t$  = time (s),  $\rho$  = fluid density ( $\text{kg m}^{-3}$ ),  $p$  = pressure (Pa),  $\mu$  = dynamic viscosity ( $\text{kg m}^{-1} \text{s}^{-1}$ ). Repeated indices imply summation. Blood was assumed to be an incompressible and Newtonian fluid [2, 34, 35] with density and viscosity being  $1060 \text{ kg m}^{-3}$  and  $0.0035 \text{ kg m}^{-1} \text{s}^{-1}$  [36] respectively. Works earlier in the literature [34] had demonstrated that intra-aneurysmal flow was not substantially altered when the viscosity model was changed. A segregated method, SIMPLE, was used as the pressure-velocity coupling scheme and first order upwind was used in momentum discretization. The time evolution of the flow was traced by a first order implicit scheme with a time step of 0.001 second. The solution at each time step was considered as converged when the residual error for continuity dropped below  $10^{-6}$ .

A pulsatile volumetric flow rate was imposed at the inlets (Fig. 4) [37]. The time-averaged flow rate was  $3.59 \text{ ml s}^{-1}$ . A different velocity inlet profile had also been tested and the results were qualitatively valid. At the outlets, a physiologically realistic pressure waveform with systolic/diastolic values of 122/82 mmHg was imposed (Fig. 5) [38]. A cardiac cycle (T) of 0.8 second was used to simulate a heartbeat rate of 75 beats per minute. Three cardiac cycles were computed and periodicity was achieved [21]. Data at the third cycle was used for analysis. Reynolds number at peak systole for all patient geometries are tabulated in Table 1. A remark on the laminar flow assumption is in order. Combined computational-experimental approaches to simulate blood flow in arteries treated by stents had been conducted in previous works in the literature [39,40]. Consistencies and agreements between these two approaches were reported, drastically enhancing the likelihood of the validity of the computational approach. Furthermore, the relevant Reynolds numbers in these previous papers and the present work are both mostly in the range of 400-700. The only possible exception is a Reynolds number of about 900 in the case for Patient 2, not too far away from the range of 400-700. Hence, with these experimental evidence and support, the usage of a laminar flow regime should be justified. The vessel wall was assumed to be rigid and a no-slip boundary condition was applied [17]. The dimensionless Womersley number [41] measures the ratio of unsteady inertia force due to pulsations to the viscous force and is defined as

$$Wo = R \sqrt{\frac{\rho \omega}{\mu}} \quad (4)$$

where  $R$  = radius (m),  $\omega$  = angular frequency ( $\text{s}^{-1}$ ),  $\rho$  = density ( $\text{kg m}^{-3}$ ) and  $\mu$  = dynamic viscosity ( $\text{kg m}^{-1} \text{s}^{-1}$ ).

#### 2.4) Hemodynamics parameters

Two hemodynamics parameters, namely energy loss (EL) [25] and volume inflow rate (VFR) into aneurysm were investigated. Energy loss (EL) estimates the pressure head loss and kinetic energy dissipation inside the vessel geometry and has a unit of Watt (W). As blood is a viscous fluid, movement through the blood vessels and aneurysm incurs an energy loss

due to viscosity. Energy loss was formulated according to Eq. (5) [22].

$$EL(t) = E(t)_{in} - E(t)_{out} = \dot{m}_{in}(p_{in}/\rho + \frac{1}{2}|u_{in}|^2) - \dot{m}_{out}(p_{out}/\rho + \frac{1}{2}|u_{out}|^2) \quad (5)$$

where  $\dot{m}$  = mass flow rate ( $\text{kg s}^{-1}$ ),  $p$  = pressure (Pa),  $|u|$  = velocity magnitude ( $\text{m s}^{-1}$ ) and  $\rho$  = fluid density ( $\text{kg m}^{-3}$ ).

Subscripts ‘in-’ or ‘out-’ denoted the inlet or outlet. The pressure and velocity magnitude as used here were area-weighted quantities. This formulation had been used earlier in literature to estimate the risk of aneurysm rupture [25]. Inserting FDs near the aneurysm orifice should in principle decrease the volume flow rate of blood passing through the aneurysm sac. Since part of the blood would not need to pass through the aneurysm, energy loss after the surgery should decrease. Quantifying the change in energy loss should reveal the effect of FDs on diverting the flow away from aneurysm sac. A parameter,  $\beta$  (Watt), will be introduced to assess the change of EL after the operation. It is defined as:

$$\beta(t) = EL(t)_{Post-operation} - EL(t)_{Pre-operation} \quad (6)$$

where  $EL$  = energy loss calculated according to Eq. (5). Subscripts ‘Pre-operation-’ or ‘Post-operation-’ denote the scenarios before and after the surgical procedure of placing the FD respectively. The relation between  $\beta$  and FDs treatment outcome has not been fully investigated, in particular, under a condition with a virtual stent. The sign of  $\beta$  would be a crucial indicator of the hemodynamic properties. To provide additional verification, a velocity inlet profile with two times the original magnitude was tested and the resultant  $\beta$  was observed to maintain the same sign.

The volume flow rate ( $\text{ml s}^{-1}$ ) passing through the aneurysm sac (VFR) was defined as the area integral of the velocity into the aneurysmal sac in a direction perpendicular to the aneurysm orifice. This parameter is a function of time and is calculated as

$$VFR(t) = \int \vec{v} \cdot d\vec{A} \quad (7)$$

where  $\vec{v}$  = velocity at the aneurysm neck orifice ( $\text{m s}^{-1}$ ),  $d\vec{A}$  = differential area of the aneurysm neck orifice ( $\text{mm}^2$ ). The area integration only included the area segment in which fluid was flowing into the aneurysm sac. Volume flow exiting the aneurysm was excluded in the integration. At any time instance, the volume flow rate into the aneurysmal sac must be equal to the volume flow rate exiting the aneurysmal sac as the sac is a domain with fixed, rigid walls. Nevertheless, this integral defined by Eq. (7) gives a measure of fluid flux into (and out of) the sac. Another quantity, VF ( $\text{ml s}^{-1}$ ), was defined as the time-averaged VFR for the whole cardiac cycle. It was calculated as

$$VF = \frac{1}{T} \int_{\tau}^{\tau+T} \int \vec{v} \cdot d\vec{A} dt \quad (8)$$

where  $\tau$  = an arbitrary time instance (s),  $T$  = cardiac cycle (s). VF was regarded as a prognostic factor for aneurysm thrombosis and reduction in flow rate was expected after a FD deployment [21, 31, 42]. Finally, results of computer

simulations including velocities and pressure were exported to MATLAB (MathWorks, Natick, MA, USA) for post-processing of CFD data.

Before presentations of the main results, a remark on the procedures used to establish accuracy quantitatively is in order. Quality assurance tests were conducted for these numerical simulations. Basically, the calculations were performed for three different mesh sizes. A refinement ratio and an observed order of convergence were determined. By assigning a safety factor, a grid convergence index was computed. Finally, the accuracy and quality of the simulations were confirmed, by combining all these parameters to conclude that the solutions were within the asymptotic range. Detailed calculations and reference was given in the Appendix.

### 3. Results

#### 3.1) Energy Loss

Four patient-specific models were chosen for this study. Their geometrical shapes, mesh elements and computational data were defined and recorded (Table 1). Two bifurcation aneurysms and two side-wall aneurysms were identified. One successful and one failed case were selected in each category. Aneurysm neck size ranges from 4.1 mm to 6.2 mm.

For Patient 1 through Patient 4, a plot of the time variation in one cardiac cycle of the values of energy loss and  $\beta$  shows that the loss occurs mainly in the systolic phase (Fig. 6). This feature holds for both the pre-operation conditions as well as the post-operation conditions. Subsequent discussions will thus focus on this regime of largest flow rates. Physically that time corresponds to  $t = 0.065$  (s). At peak systole, energy loss for the pre-operation case ranges from 3.12 (milli-Watt) to 43.12 (milli-Watt) (Table 3).  $\beta$  ranges from -1.328 (milli-Watt) to 0.076 (milli-Watt) (Table 3). After FD deployment, successful cases display negative  $\beta$  at peak systole while the failed cases possess positive  $\beta$  in this peak flow phase.

A remark on the underlying reasoning in terms of hemodynamics is in order. In a viscous flow, energy is always dissipated in moving a fluid against internal friction. For the present situation of cerebral aneurysm, a successful surgical intervention will imply less blood flow into aneurysmal sac, resulting in less energy loss or a negative  $\beta$ . On the other hand, a failed surgical procedure is usually associated with sustained flow in the sac. Moreover, the fluid must squeeze through the small apertures on the flow diverter too, resulting in more energy dissipation and thus a positive  $\beta$ . The geometry of Patient 2 exhibited a relatively higher change in energy loss as compared with the other three geometries because of its small size (Table 1). Viscosity in blood would result in an energy loss and a smaller geometric size would amplify this effect. Figure 7 shows the streamlines at peak systole for Patient 1 through Patient 4. In general, blood was diverted away from the aneurysm sac after FD deployment. A common conjecture is that a slower flow rate in the aneurysm may promote the chance of thrombosis and

clotting.

### 3.2) Volume flow rate (VFR)

Volume flow rate into aneurysm was reduced for all four patient cases after FD deployment. Reductions of volume flow rate into aneurysm were again concentrated in the systolic phase (Fig. 8), and the decrease in time-averaged volume flow rate, VF, ranged from 45% to 78% (Table 3). Percentage change in VF after FDs deployment did not show a discriminative trend between successful cases and failed cases. FDs served their purpose in this aspect. They drastically reduce blood flow into the aneurysm sac.

### 3.3) Comparison between modeling a FD as a virtual stent versus a porous medium

Patient 1 was a successful case while Patient 3 was a failed case. Geometric configurations of bifurcation aneurysm of Patients 1 and sidewall aneurysm of Patient 3 were further modeled as a porous medium, employing the formulations of Section 2.2. More precisely, simulations using two sets of parameters corresponding to ‘tangential orientation’ and ‘normal orientation’ [32] were compared with those from virtual stent deployment, in terms of streamlines plots (Fig. 9).

Although the patterns might look qualitatively similar, a more quantitative assessment can be made by defining a dimensionless parameter  $\gamma$  which measures the effective inflow volume flux ratio of the blood into aneurysmal sac as

$$\gamma = \frac{\vec{v} \cdot \vec{A}}{\|\vec{v}\| \|\vec{A}\|} \quad (9)$$

where  $\vec{v}$  = inflow velocity vector on the neck orifice ( $\text{m s}^{-1}$ ),  $\vec{A}$  = area vector normal to the neck orifice ( $\text{mm}^2$ ). The area-weighted average of  $\gamma_{\text{average}}$  is defined as

$$\frac{\int \gamma dA}{\int dA} \quad (10)$$

In other words,  $\gamma_{\text{average}}$  measures the averaged effective inflow volume flux ratio into the aneurysmal sac. Mathematically  $0 < \gamma_{\text{average}} < 1$ , and a value of unity is attained only if the inflow velocity is everywhere perpendicular to the surface area of the orifice. Data from Patient 1 demonstrate that the virtual stent scheme generally permits a higher effective volume influx ratio than those from the porous medium approximations (Fig. 10). Although the virtual stent scheme is likely to provide a more realistic description of the flow, the actual verification might require an experimental or clinical measurement. Indeed this feature is also reflected in the streamline patterns of Fig. 8, where the streamlines of the virtual stent case are more likely to enter the sac in a direction perpendicular to the stent surface.

Table 4 shows the VFR (volume flow rate at peak systole) and VF (volume flow rate averaged over one period) of the pre-operation and post-operation stages for both Patients 1 and 3. The post-operation stage includes all three versions considered, namely, virtual stent, porous medium: ‘tangential orientation’, and porous medium: ‘normal orientation’. In terms of percentages, VF reductions range from 54.3% to 78.4% for Patient 1, and 71.6% to 77.3% for Patient 3. The corresponding trends for volume flow rate at peak systole are 38.7% to 65.6% for Patient 1, and 59.8% to 73.3% for Patient 3. Hence values of these reductions can differ from each other by as much as 27%, depending on the precise modeling techniques employed. In particular, for Patient 3, the porous medium approximation (‘tangential orientation’) displays a higher reduction of volume flow rate at peak systole than virtual stent case. However, the virtual stent has a higher overall VF reduction. Flow patterns simulated by the virtual stent and porous medium scenarios can thus be drastically different.

A plot of the parameter  $\beta$  (difference of energy loss between pre-operation and post-operation) versus time shows similar pattern for both Patient 1 and Patient 3 (Fig. 11). The actual values of energy loss and  $\beta$  are also tabulated (Table 5). In terms of percentages of the pre-operation values of energy loss,  $\beta$  ranges from -2.62% to -1.55% for Patient 1, and -0.31% to 1.76% for Patient 3. The remarkable feature occurs for Patient 3, where the sign of the parameter  $\beta$  for the virtual stent modeling and porous media approximations are *different*, highlighting the fact that the mode of modeling may have an important bearing on the computational results. The flow patterns inside the aneurysm for the virtual stent case and the porous medium scheme are different from each other too.

#### 4. Discussion

The energy loss parameter  $\beta$  (Eq. (6)) at peak systole exhibits a notable difference between the clinically successful cases and failed cases. Figure 6 and Table 3 reflect this difference in medical outcomes after stent deployment. A qualitative explanation can be put forward to elucidate this correlation with clinical outcome. For a successful flow diverter treatment of intracranial aneurysm, most blood will flow along the parent vessel instead of a ‘longer’ route into the aneurysm. Hence, less energy should be dissipated and  $\beta$  should be negative (Eq. (6)). However, for a failed clinical procedure, where a significant amount of blood still maintains a circulation within the sac, the blood will need to be squeezed through the stent pores (Fig. 7). This scenario results in more energy loss and leads to a positive value for  $\beta$  after stenting. Hence, by examining the sign of  $\beta$ , prediction and correlation of treatment outcome may be possible.

In the current study, both side-wall and bifurcation aneurysms were investigated. They corresponded to two different forms of aneurysm which would induce different flow patterns. Under this condition, the selected successful and failed cases display negative and positive values of  $\beta$  respectively, regardless of the shape and size of aneurysm. Nevertheless, only a few selected patients were tested in this preliminary study and more data will need to be collected before a definitive conclusion

can be drawn on using  $\beta$  to correlate with treatment outcomes.

To contrast the flow patterns into the sac for the virtual stent and porous media cases, quantitative indicators are defined. Parameters for porous medium modeling perhaps need to be adjusted carefully, depending on the orientation of the stent and setting of the simulation. Experimental flow visualization or clinical measurement might be needed in the future to assess the most accurate or reliable model to be utilized. In terms of viscosity model, a previous work in the literature [34] indicated that the intra-aneurysmal flow was not altered substantially by the change of viscosity model and wall shear stress data on cerebral aneurysm were taken from a CFD study [35] performed by using Newtonian fluid. However, in regions with slow blood flow or vessels of dimensions smaller than those considered here, non-Newtonian properties will become important [33]. The effect of non-Newtonian properties [43] on the energy loss parameter will be left for further study.

Further on the issue of volume inflow rate to aneurysm, a porous medium model can reproduce the volume flow rate and VF reduction. However, the time evolution of volume flow rate and magnitude in reduction of this model were significantly different from virtual stent cases which can be shown in (Fig. 11). Furthermore, the values of the parameter  $\beta$  at peak systole after the operation in Patient 3 calculated from the virtual stent model and the porous medium approximation display *different* signs. This difference implies that the choice of modeling techniques could have a large influence on the value of  $\beta$ . Hence, a porous medium approximation should be implemented carefully. On the other hand, in a virtual stent simulation, porosity plays a pivotal role [21], the determination and analysis of stent porosity in the numerical simulations should be verified experimentally or clinically if possible.

## 5. Conclusions

The present study focuses on the computer simulations of the hemodynamics of cerebral aneurysms, both before and after flow diverter stent deployment. The energy loss parameter measures the work necessary to push fluid from one point to another through the viscous resistance of the fluid. A successful surgical procedure would lead to less blood flow into the sac and more fluid moving along the parent vessel, resulting in a smaller amount of energy loss. Hence the parameter  $\beta$ , defined as the difference between the post-operation and pre-operation values of the energy loss for the same patient, should be negative for a successful surgical procedure. On the other hand, a significant persisting flow into the aneurysm is usually associated with a failed surgical procedure. Blood squeezing through the stent will imply a larger energy loss, and hence  $\beta$  should be positive for such unsuccessful treatment. Our findings were consistent with previous studies [13]. Nevertheless, more patient data need to be collected and tested, before this energy loss parameter can become a reliable clinical indicator.

A remark on the constraint or limitations of the present approach is appropriate. Blood flow is in general unsteady, three

dimensional (or helical), and often in turbulent or transitional state. The complex geometry of vessels aggravates the situation. Hence a simple indicator like the energy loss parameter is unlikely to be universally applicable. Indeed, it is intended as a ‘conservative’ measure to highlight a trend which hopefully provides useful insight in most clinical applications.

Technically the refined and improved aspect in the analysis implemented in this work is that a virtual stent is employed in the simulations, instead of a porous medium approximation. This action should serve as a more realistic description. When flows are described by a porous medium approach, different sets of input parameter values are possible, arising from the approximate orientation schemes used. Depending on this choice, the signs of  $\beta$  can be positive and negative. Furthermore, the flow patterns computed from the porous medium and virtual stent schemes are different. Hence, clinical as well as experimental verifications are needed in the future.

**Acknowledgments** Partial financial support was provided by the Innovation and Technology Support Program (ITS/150/15) of the Hong Kong Special Administrative Region Government.

**Conflict of Interest:** The authors declare that they have no conflict of interest.

## Appendix

Some technical details concerning the quality assurance on the accuracy of the simulations would be given here. Two columns of data were listed in the following table which described the number of cells used in all the meshes utilized. The parameter ‘Energy Loss’ was calculated at a time instance when  $\beta$  has the largest variation across different meshes. The adjectives, ‘Large’, ‘Medium’ and ‘Small’ were then used to designate these meshes. According to [44], Grid Convergence Index (GCI) was calculated and recorded for one of the cases.

Case 1 – Successful case

Case 1a: Pre-operation

Details of grid size was tabulated in Table 6. Number of cells utilized in the study = 539,662

The ‘Energy Loss’ parameter was thus quite insensitive to the number of cells (error < 0.5%) once a threshold is reached, a feature also illustrated in Fig. 12.

### *Analysis*

The refinement ratio  $r$  was approximately 1.44, while the observed order of convergence  $p$  was very close to 2.50. For the three-grid study, a factor of safety ( $F_s$ ) given by  $F_s = 1.25$  was used for calculating grid convergence index (GCI) for the finer grids [44]. Employing these established procedures, standard calculations yielded:

$$GCI_{\text{Medium-Small}} = 0.459\% , \quad GCI_{\text{Large-Medium}} = 1.136\% .$$

A quality assurance check was conducted to test if the solutions were in the asymptotic range:

$$GCI_{\text{Medium-Small}} / (r^p GCI_{\text{Large-Medium}}) = 0.9946 .$$

This value of approximately unity thus confirmed that the solution was within the appropriate asymptotic range. Similar patterns are observed in other simulations reported in the text.

## References

1. Vlak, M. H., Algra, A., Brandenburg, R., Rinkel, G. J. (2011). Prevalence of unruptured intracranial aneurysms, with emphasis on sex, age, comorbidity, country, and time period: a systemic review and meta-analysis. *The Lancet Neurology*, 10(7), 626-636.
2. Humphrey, J. D., Taylor, C. A. (2008). Intracranial and abdominal aortic aneurysms: similarities, differences, and need for a new class of computational models. *Annual Review of Biomedical Engineering*, 10, 221-246.
3. Pierot, L., Cognard, C., Anxionnat, R., Ricolfi, F. (2012). Endovascular treatment of ruptured intracranial aneurysms: factors affecting midterm quality anatomic results: analysis in a prospective, multicenter series of patients (CLARITY). *American Journal of Neuroradiology*, 33(8), 1475-1480.
4. Gonzalez, N. R., Duckwiler, G., Jahan, R., Murayama, Y., Viñuela, F. (2006). Challenges in the endovascular treatment of giant intracranial aneurysms. *Neurosurgery*, 59(5), S3-113.
5. Jou, L., Mawad, M. (2011). Timing and size of flow impingement in a giant intracranial aneurysm at the internal carotid artery. *Medical & Biological Engineering & Computing*, 49(8), 891-899.
6. Leung, G., Tsang, A., Lui, W. (2012). Pipeline embolization device for intracranial aneurysm: a systematic review. *Clinical Neuroradiology*, 22(4), 295-303.
7. Shapiro, M., Raz, E., Becske, T., Nelson, P. (2014). Variable porosity of the pipeline embolization device in straight and curved vessels: a guide for optimal deployment strategy. *American Journal of Neuroradiology*, 35(4), 727-733.
8. Byrne, J., Beltechi, R., Yarnold, J., Birks, J., Kamran, M. (2010). Early experience in the treatment of intra-cranial aneurysms by endovascular flow diversion: a multicentre prospective study. *PloS ONE*, 5(9), e12492.
9. Wang, C., Tian, Z., Liu, J., Jing, L., Palival, N., Zhang, Y., Xiang, J., Siddiqui, A. H., Meng, H., Wang, S., Yang, X. (2016). Hemodynamic Alterations for Various Stent Configurations in Idealized Wide-neck Basilar Tip Aneurysm. *Journal of Medical and Biological Engineering*, 36(3), 379-385.
10. Kallmes, D., Ding, Y., Dai, D., Kadirvel, R., Lewis, D., Cloft, H. (2009). A second-generation, endoluminal, flow-disrupting device for treatment of saccular aneurysms. *American Journal of Neuroradiology*, 30(6), 1153-1158.
11. Brinjikji, W., Murad, M., Lanzino, G., Cloft, H., Kallmes, D. (2013). Endovascular treatment of intracranial aneurysms with flow diverters a meta-analysis. *Stroke*, 44(2), 442-447.
12. Caruso, M. V., Gramigna, V., Serraino, G. F., Renzulli, A., Fragomeni, G. (2015). Influence of Aortic Outflow Cannula Orientation on Epiaortic Flow Pattern During Pulsed Cardiopulmonary Bypass. *Journal of Medical and Biological Engineering*, 35(4), 455-463.
13. Cebral, J., Mut, F., Weir, J., Putman, C. (2011). Quantitative characterization of the hemodynamic environment in ruptured and unruptured brain aneurysms. *American Journal of Neuroradiology*, 32(1), 145-151.
14. Lee, C.J., Zhang, Y., Takao, H., Murayama, Y., Qian, Y. (2013). A fluid-structure interaction study using patient-specific ruptured and unruptured aneurysm: The effect of aneurysm morphology, hypertension and elasticity. *Journal of Biomechanics*, 46(14), 2402-2410.
15. Takao, H., Murayama, Y., Otsuka, S., Qian, Y., Mohamed, A., Masuda, S., Yamamoto, M., Abe, T. (2012). Hemodynamic differences between unruptured and ruptured intracranial aneurysms during observation. *Stroke*, 43(5), 1436-1439.
16. Li, G., Hu, R., Gao, F. (2015). Numerical Simulation of Coronary Artery Stenosis Before and After Stenting. *Journal of Medical and Biological Engineering*, 35(4), 528-534.
17. Cebral, J., Mut, F., Raschi, M., Scrivano, E., Ceratto, R., Lylyk, P., Putman, C. (2011). Aneurysm rupture following treatment with flow-diverting stents: computational hemodynamics analysis of treatment. *American Journal of Neuroradiology*, 32(1), 27-33.
18. Goubergrits, L., Schaller, J., Kertzscher, U., Woelken, T., Ringelstein, M., Spuler, A. (2014). Hemodynamic impact of cerebral aneurysm endovascular treatment devices: coils and flow diverters. *Expert Review of Medical Devices*, 11(4), 361-373.
19. Kim, Y.H., Xu, X., Lee, J.S. (2010). The effect of stent porosity and strut shape on saccular aneurysm and its numerical analysis with lattice Boltzmann method. *Annals of Biomedical Engineering*, 38(7), 2274-2292.
20. Kulcsár, Z., Augsburger, L., Reymond, P., Pereira, V.M., Hirsch, S., Mallik, A.S., Millar, J., Wetzel, S.G., Wanke, I., Rufenacht, D.A. (2012). Flow diversion treatment: intra-aneurismal blood flow velocity and WSS reduction are parameters to predict aneurysm thrombosis. *Acta Neurochirurgica*, 154(10), 1827-1834.
21. Tang, A. Y. S., Chung, W. C., Liu, E. T. Y., Qu, J. Q., Tsang, A. C. O., Leung, G. K. K., Leung, K. M., Yu, A. C. H., Chow, K. W. (2015). Computational Fluid Dynamics Study of Bifurcation Aneurysms Treated with Pipeline Embolization Device: Side Branch Diameter Study. *Journal of Medical and Biological Engineering*, 35(3), 293-304.
22. Chong, W., Zhang, Y., Qian, Y., Lai, L., Parker, G., Mitchell, K. (2014). Computational hemodynamics analysis of intracranial aneurysms treated with flow diverters: correlation with clinical outcomes. *American Journal of Neuroradiology*, 35(1), 136-142.
23. Xiang, J., Damiano, R. J., Lin, N., Snyder, K. V., Siddiqui, A. H., Levy, E. I., Meng, H. (2015). High-fidelity virtual stenting: modeling of flow diverter deployment for hemodynamic characterization of complex intracranial aneurysms. *Journal of Neurosurgery*, 123(4), 832-840.
24. Zhang, Y., Chong, W., Qian, Y. (2013). Investigation of intracranial aneurysm hemodynamics following flow diverter stent treatment. *Medical Engineering & Physics*, 35(5), 608-615.
25. Qian, Y., Takao, H., Umezawa, M., Murayama, Y. (2011). Risk analysis of unruptured aneurysms using computational fluid dynamics technology: preliminary results. *American Journal of Neuroradiology*, 32(10), 1948-1955.
26. Hu, P., Qian, Y., Lee, C., Zhang, H., Ling, F. (2015). The energy loss may predict rupture risks of anterior communicating aneurysms: a preliminary result. *International Journal of Clinical and Experimental Medicine*, 8(3), 4128-4133.
27. Liu, J., Xiang, J., Zhang, Y., Wang, Y., Li, H., Meng, H., Yang, X. (2014). Morphologic and hemodynamic analysis of paraclinoid aneurysms: ruptured versus unruptured. *Journal of Neurointerventional Surgery*, 6, 658-663.
28. Farnoush, A., Avolio, A., Qian, Y. (2013). Effect of bifurcation angle configuration and ratio of daughter diameters on hemodynamics of bifurcation aneurysms. *American Journal of Neuroradiology*, 34(2), 391-396.
29. Farnoush, A., Avolio, A., Qian, Y. (2014). A growth model of saccular aneurysms based on hemodynamic and morphologic discriminant parameters for risk of rupture. *Journal of Clinical Neuroscience*, 21(9), 1514-1519.
30. Ren, X., Qiao, A., Song, H., Song, G., Jiao, L. (2016). Influence of Bifurcation Angle on In-Stent Restenosis at the Vertebral Artery Origin: A Simulation Study of Hemodynamics. *Journal of Medical and Biological Engineering*, 36(4), 555-562.
31. Tsang, A. C., Tang, A. Y., Chung, W.C., Leung, G. K., Chow, K.W. (2016). Correlating Hemodynamic Changes and Occlusion Time after Flow Diverter Treatment of Bilateral Large Internal Carotid Artery Aneurysms. *Clinical Neuroradiology*, 26(4), 477-480.
32. Augsburger, L., Reymond, P., Rufenacht, D., Stergiopoulos, N. (2011). Intracranial stents being modeled as a porous medium: flow simulation in stented cerebral aneurysms. *Annals of Biomedical Engineering*, 39(2), 850-863.
33. Sforza, D., Putman, C., Cebral, J. (2009). Hemodynamics of cerebral aneurysms. *Annual Review of Fluid Mechanics*, 41, 91-107.
34. Cebral, J. R., Castro, M. A., Appanaboyina, S., Putman, C. M., Millan, D., Frangi, A. F. (2005). Efficient pipeline for image-based patient-specific analysis of cerebral aneurysm hemodynamics: technique and sensitivity. *IEEE Transactions on Medical Imaging*, 24(4), 457-467.
35. Shojima, M., Oshima, M., Takagi, K., Torii, R., Hayakawa, M., Katada, K., Morita, A., Kirino, T. (2004). Magnitude and role of wall shear stress on cerebral aneurysm - Computational fluid dynamic study of 20 middle cerebral artery aneurysms. *Stroke*, 35(11), 2500-2505.
36. Marzo, A., Singh, P., Larribide, I., Radaelli, A., Coley, Coley, S., Gwilliam, M., Wilkinson, I. D., Lawford, P., Reymond, P., Patel, U., Frangi, A. (2011). Computational hemodynamics in cerebral aneurysms: the effects of modeled versus measured boundary conditions. *Annals of Biomedical Engineering*, 39(2), 884-896.

37. Ku, D., Giddens, D., Zarins, C., Glagov, S. (1985). Pulsatile flow and atherosclerosis in the human carotid bifurcation. Positive correlation between plaque location and low oscillating shear stress. *Arteriosclerosis, Thrombosis, and Vascular Biology*, 5(3), 293-302.
38. Reymond, P., Bohraus, Y., Perren, F., Lazeyras, F., Stergiopoulos, N. (2011). Validation of a patient-specific one-dimensional model of the systemic arterial tree. *American Journal of Physiology-Heart and Circulatory Physiology*, 301(3), H1173-H1182.
39. Benard, N., Coisne, D., Donal, E., Perrault, R. (2003). Experimental study of laminar blood flow through an artery treated by a stent implantation: characterisation of intra-stent wall shear stress. *Journal of Biomechanics*, 36(7), 991-998.
40. Berg, P., Iosif, C., Ponsonnard, S., Yardin, C., Janiga, G., Mounayer, C. (2016). Endothelialization of over-and undersized flow-diverter stents at covered vessel side branches: An in vivo and in silico study. *Journal of Biomechanics*, 49(1), 4-12.
41. Womersley, J. R. (1955). Method for the calculation of velocity, rate of flow and viscous drag in arteries when the pressure gradient is known. *The Journal of Physiology*, 127(3), 553-563.
42. Pereira, V., Bonnefous, O., Ouared, R., Brina, O., Stawiaski, J., Aerts, H., Ruijters, D., Narata, A. P., Bijlenga, P., Schaller, K., Lovblad, K. (2013). A DSA-based method using contrast-motion estimation for the assessment of the intra-aneurysmal flow changes induced by flow-diverter stents. *American Journal of Neuroradiology*, 34(4), 808-815.
43. Carty, G., Chatpun, S., Espino, D. M. (2016). Modeling blood flow through intracranial aneurysms: a comparison of Newtonian and non-Newtonian viscosity. *Journal of Medical and Biological Engineering*, 36(3), 396-409.
44. ASME V&V 20 (2009). Standard for Verification and Validation in Computational Fluid Dynamics and Heat Transfer. New York, NY: American Society of Mechanical Engineers.

## Figure legends

Fig. 1 Patient-specific geometries,(a)-(d), ranging from Patient 1 to Patient 4 for performing CFD simulations , (*left column*) Pre-operation condition, (*right column*) Post-operation condition, solid arrow indicates the inlet position, hollow arrow(s) indicate(s) outlet position(s), dash line(s) indicate(s) aneurysm or flow diverter

Fig. 2 Detail configuration of a stent unit of PED [7]

Fig. 3 Illustration of the additional pressure drop term on porous medium modeling, refer to Eq. (1) for abbreviations.

Fig. 4 Pulsatile blood volume flow rate imposed at the inlet [37], the cross indicates peak systole

Fig. 5 Physiologically realistic pressure waveform which simulates the physiological condition imposed at outlet(s) [38]

Fig. 6 Time evolution of energy loss for each case – (*left column*) pre-operation condition, (*right column*)  $\beta$ , as defined in Eq. (6), a measure of energy loss, after inserting a virtual stent: Successful cases have a negative  $\beta$  at peak systole while failed cases have positive  $\beta$  (a) Patient 1, Successful case (b) Patient 2, Successful case (c) Patient 3, Failed case (d) Patient 4, Failed case

Fig. 7 Streamline plot of each case at peak systole, (*left column*) Streamline before stenting, (*right column*) Streamline after inserting virtual stent which indicates a reduction in volume flow, (a) Patient 1, Successful case (b) Patient 2, Successful case (c) Patient 3, Failed case (d) Patient 4, Failed case

Fig. 8 Time evolution of volume flow rate into aneurysm (a) Patient 1, Successful case (b) Patient 2, Successful case (c) Patient 3, Failed case (d) Patient 4, Failed case

Fig. 9 Streamline plots of different modeling techniques at peak systole for (*left column*) Patient 1 & (*right column*) Patient 3 (a) FD modeled as a virtual stent (b) FD modeled by porous medium (parameters as adopted from the ‘Tangential Orientation’ approximation) [32] (c) FD modeled by porous medium (parameters as adopted from the ‘Normal Orientation’ approximation) [32]

Fig. 10 Time evolution of the area-weighted average volume influx parameter ( $\gamma$ ) for the post-operation geometry of Patient 1 with different modeling techniques, namely, virtual stent, porous medium with ‘Tangential Orientation’ and ‘Normal Orientation’ parameters [32]

Fig. 11 Comparison between different flow-diverter modeling techniques and parameters, namely, virtual stent, porous medium with ‘tangential orientation’ parameters & porous medium with ‘normal orientation’ parameters [32] (a) volume flow rate into aneurysm (b)  $\beta$ , as defined in Eq. (6), a measure of energy loss, (*left column*) Patient 1, (*right column*) Patient 3

Fig. 12 Energy loss for the pre-operation condition for different mesh sizes versus time in one cardiac cycle for Patient 1

## **Table legends**

Table 1 Patient-specific geometries information, number of tetrahedral elements and flow parameters

Table 2 Porous medium parameters modeling FDs [32]

Table 3 Energy loss at peak systole and time-averaged volume flow rate passing aneurysm sac for successful cases and failed cases

Table 4 Volume flow rates of different post-operation modeling and their percentage difference with the pre-operation case

Table 5 Energy loss at peak systole for pre-operation and different post-operation modeling and the corresponding  $\beta$ s

Table 6 Number of cells and corresponding energy loss for different meshes

Table 7 Patient-specific geometries information, number of tetrahedral elements and flow parameters

Patient	1	2	3	4
Aneurysm type	Bifurcation	Side-wall	Bifurcation	Side-wall
Volume (mm <sup>3</sup> )	43	10	127	201
Aneurysm neck size (mm)	6.2	4.1	5.9	4.2
Treatment outcome	Successful	Successful	Failed	Failed
Number of elements (Pre-operation case)	539,662	115,890	212,642	687,787
Number of elements (Post-operation case)	2,265,762	2,539,721	3,000,236	2,419,143
Porosity (%)	75.5	74.5	72.8	72.5
Reynolds number (Re)	452	910	678	516
Womersley number (Wo)	4.6	2.2	3.0	4.0

Table 8 Porous medium parameters modeling FDs [32]

Orientation of FDs	Viscous resistance		Pressure-jump coefficient	
	$1/\alpha$ (m <sup>-2</sup> )		$C$ (m <sup>-1</sup> )	
	Tangential Orientation	Normal Orientation	Tangential Orientation	Normal Orientation
Porous medium parameters	1.7*10 <sup>9</sup>	8.9*10 <sup>8</sup>	4,697	8,703

Table 9 Energy loss at peak systole and time-averaged volume flow rate passing aneurysm sac for successful cases and failed cases

Patient (Clinical Outcome)	Energy Loss at peak systole		$\beta$ (milli-Watt) [% w.r.t pre-operation Energy Loss]	VF (Volume flow rate averaged over one period)		
	Pre-operation (milli-Watt)	Post-operation (milli-Watt)		Pre-operation (milli-liter s <sup>-1</sup> )	Post-operation (milli-liter s <sup>-1</sup> )	Percentage change (%)
1 (Successful)	5.21	5.08	-0.136 [-2.62%]	1.094	0.236	-78.4
2 (Successful)	43.12	41.79	-1.328 [-3.08%]	0.991	0.547	-44.8
3 (Failed)	4.30	4.38	0.076 [+1.76%]*	1.611	0.366	-77.3
4 (Failed)	3.12	3.20	0.075 [+2.41%]*	0.512	0.155	-69.7

\* Positive  $\beta$  represented higher energy loss was needed to push the blood through the vessel system after stent deployment

Table 10 Volume flow rates of different post-operation modeling and their percentage difference with the pre-operation case

	VF (milli-liter s <sup>-1</sup> ) (volume flow rate averaged over one period)	Percentage difference	VFR (milli-liter s <sup>-1</sup> ) (volume flow rate at peak systole)	Percentage (%)
<b>Patient 1</b>				
Pre-operation	1.094	N/A	2.265	N/A
Virtual stent	0.236	-78.4	0.779	-65.6
Porous medium (‘Tangential Orientation’)	0.340	-68.9	1.046	-53.8
Porous medium (‘Normal Orientation’)	0.500	-54.3	1.389	-38.7
<b>Patient 3</b>				
Pre-operation	1.611	N/A	3.328	N/A
Virtual stent	0.366	-77.3	0.964	-71.0
Porous medium (‘Tangential Orientation’)	0.368	-77.1	0.889	-73.3
Porous medium (‘Normal Orientation’)	0.457	-71.6	1.339	-59.8

Table 11 Energy loss at peak systole for pre-operation and different post-operation modeling and the corresponding  $\beta$ s

	Energy Loss (milli-Watt)	$\beta$ (milli-Watt) [% w.r.t pre-operation Energy Loss]
<b>Patient 1</b>		
Pre-operation	5.21	N/A
Virtual stent	5.08	-0.136 [-2.62%]
Porous medium (‘Tangential Orientation’)	5.09	-0.127 [-2.44%]
Porous medium (‘Normal Orientation’)	5.13	-0.081 [-1.55%]
<b>Patient 3</b>		
Pre-operation	4.30	N/A
Virtual stent	4.38	0.076 [+1.76%]
Porous medium (‘Tangential Orientation’)	4.29	-0.014 [-0.31%]*
Porous medium (‘Normal Orientation’)	4.29	-0.010 [-0.23%]*

\* $\beta$  has different signs

Table 6 Number of cells and corresponding energy loss for different meshes

Grid size	Number of cells	Energy loss (milli-Watt)
Large	361*103	3.28
Medium	540*103	3.23
Small	750*103	3.22

Fig1

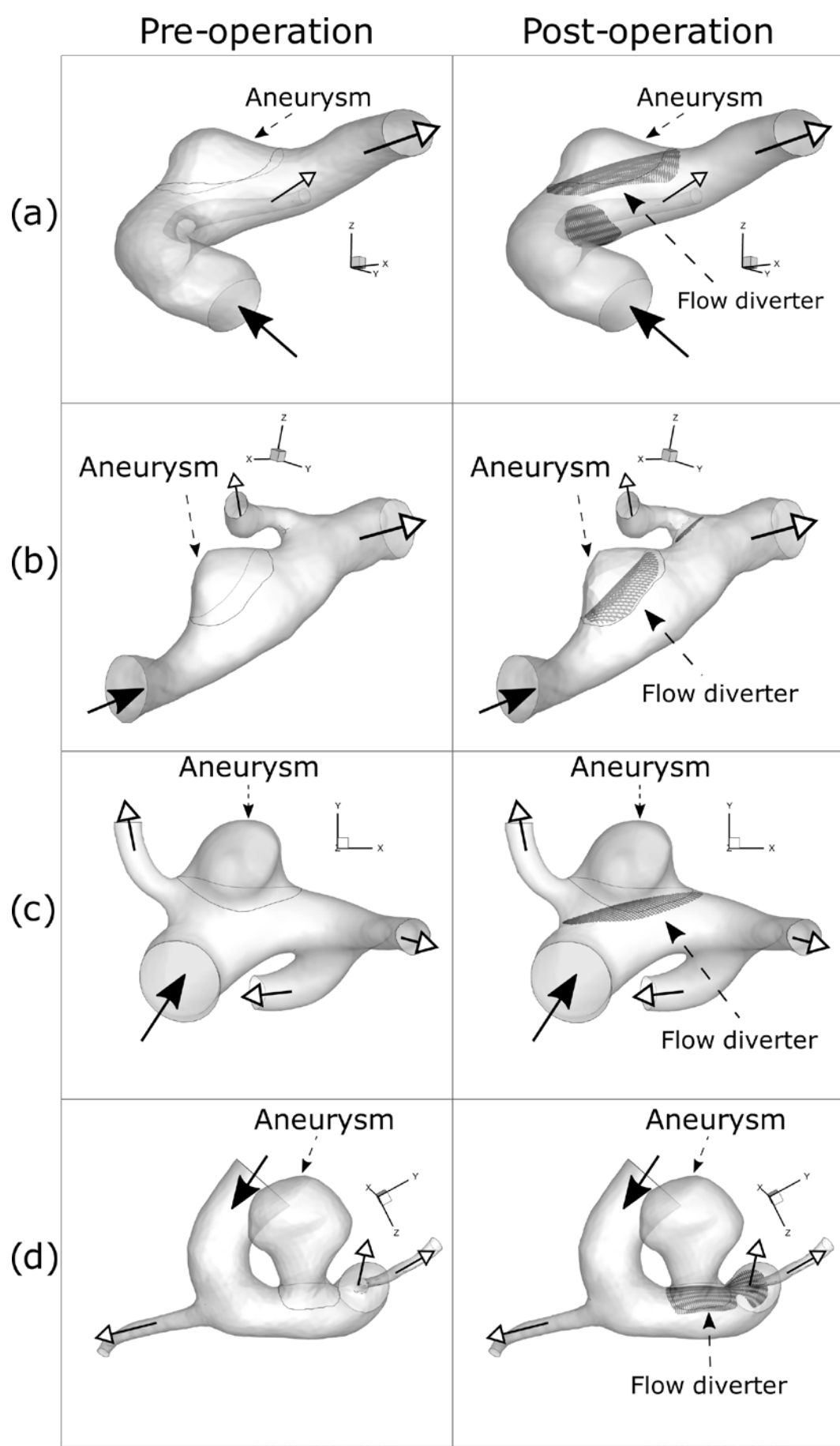


Fig2

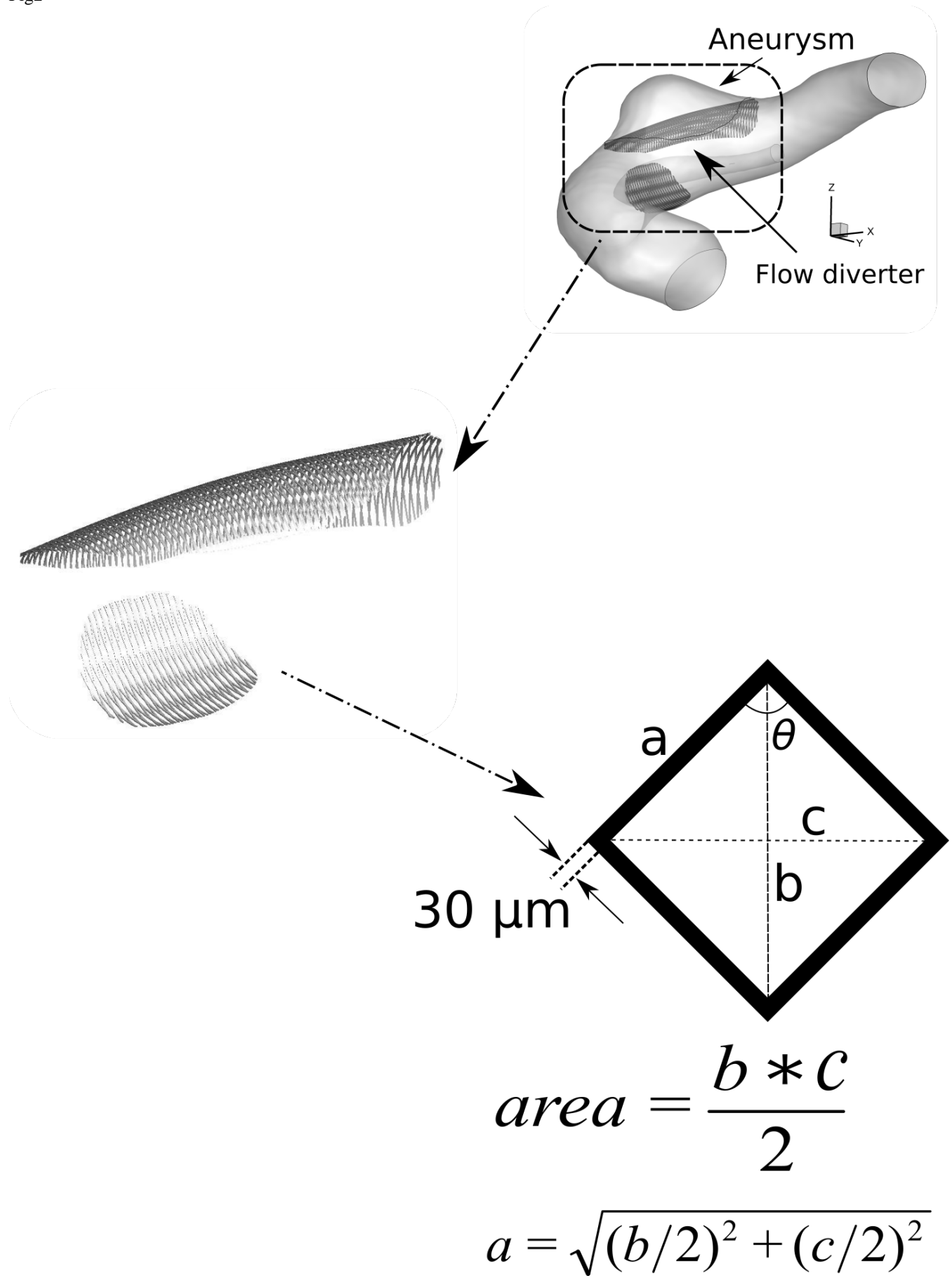
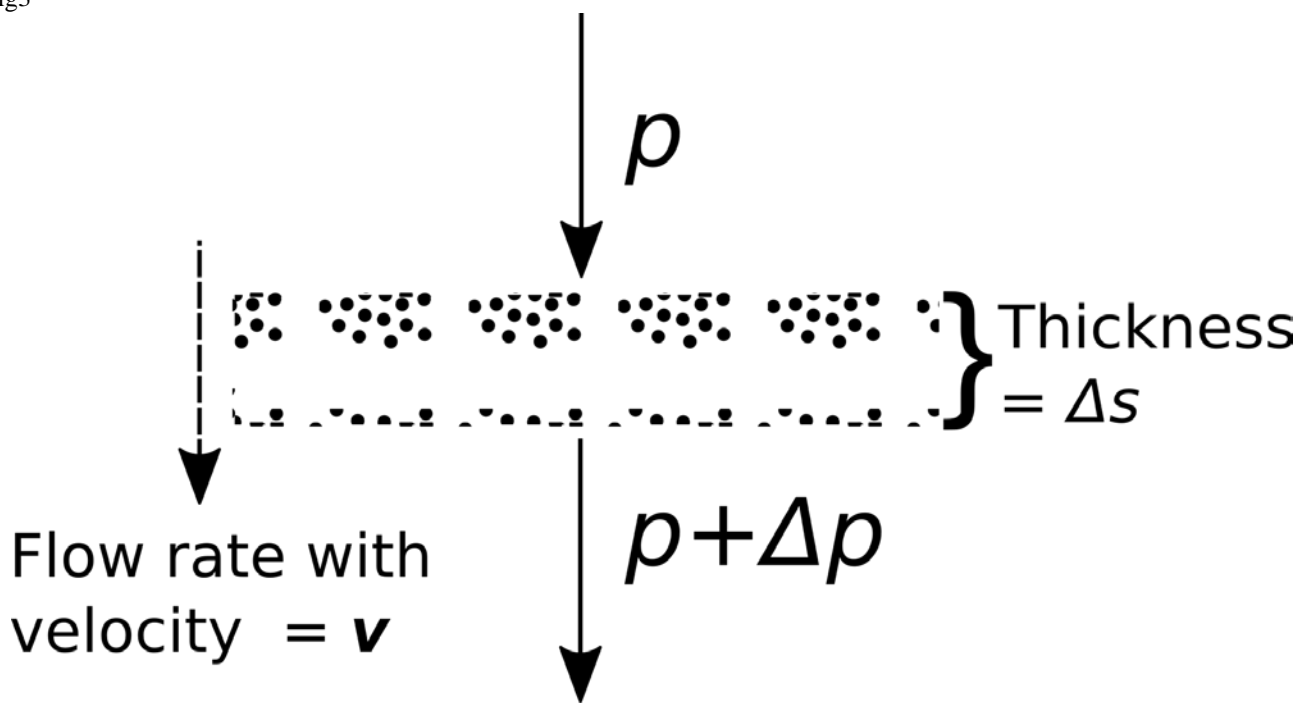


Fig3



$$\Delta p = -\left(\frac{\mu}{\alpha} v + C \frac{1}{2} \rho v^2\right) \Delta s$$

Fig4

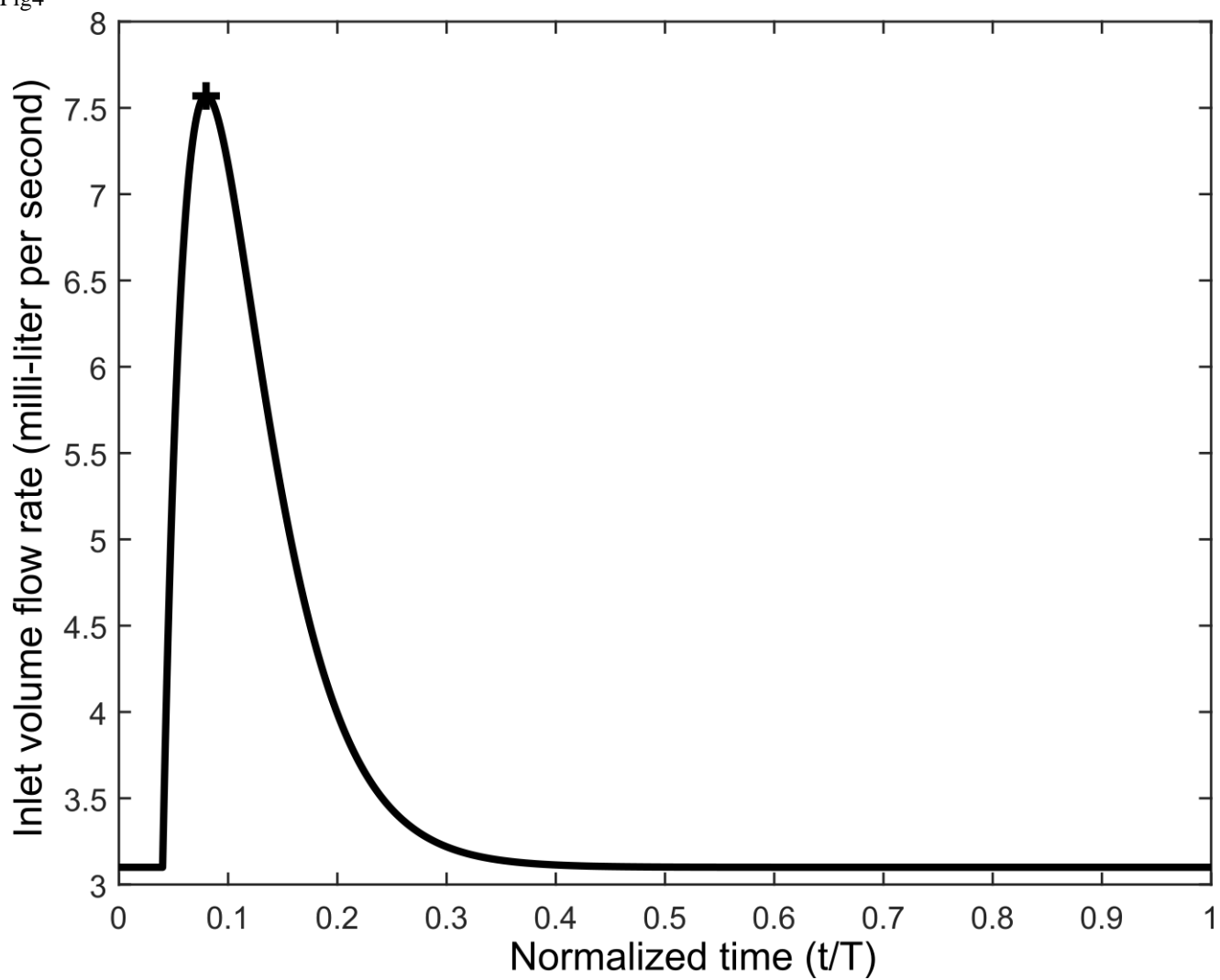


Fig5

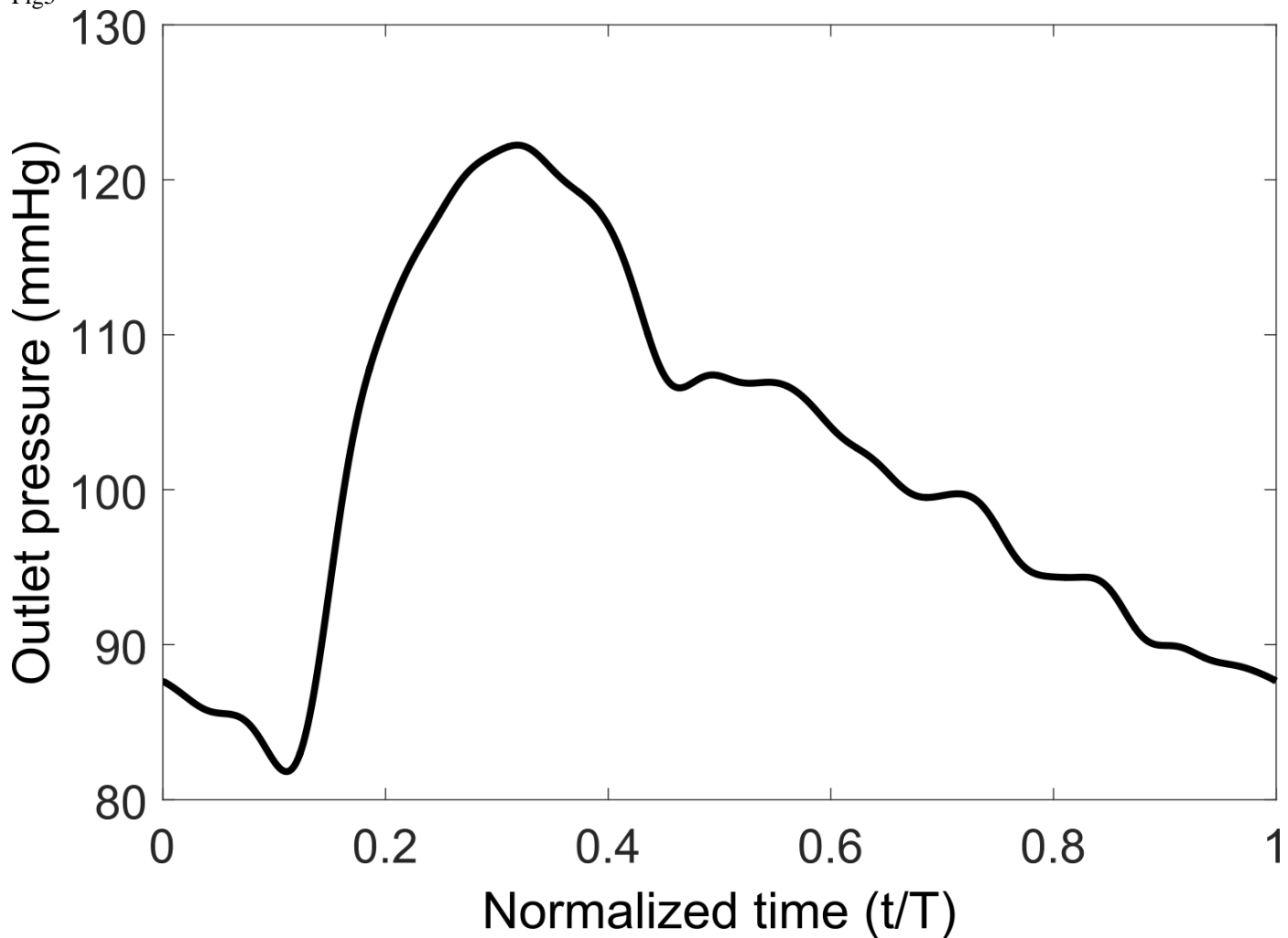


Fig6

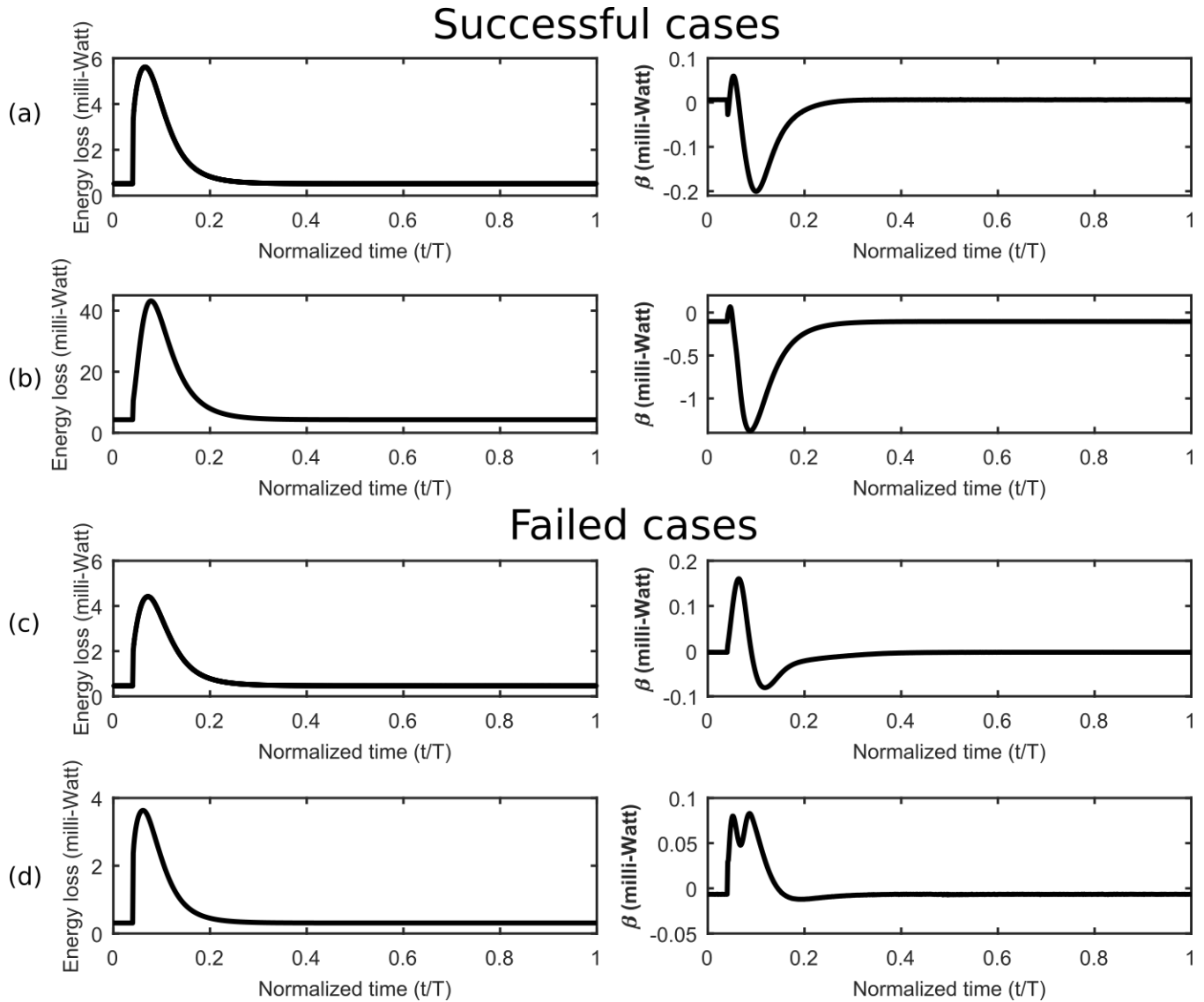


Fig7

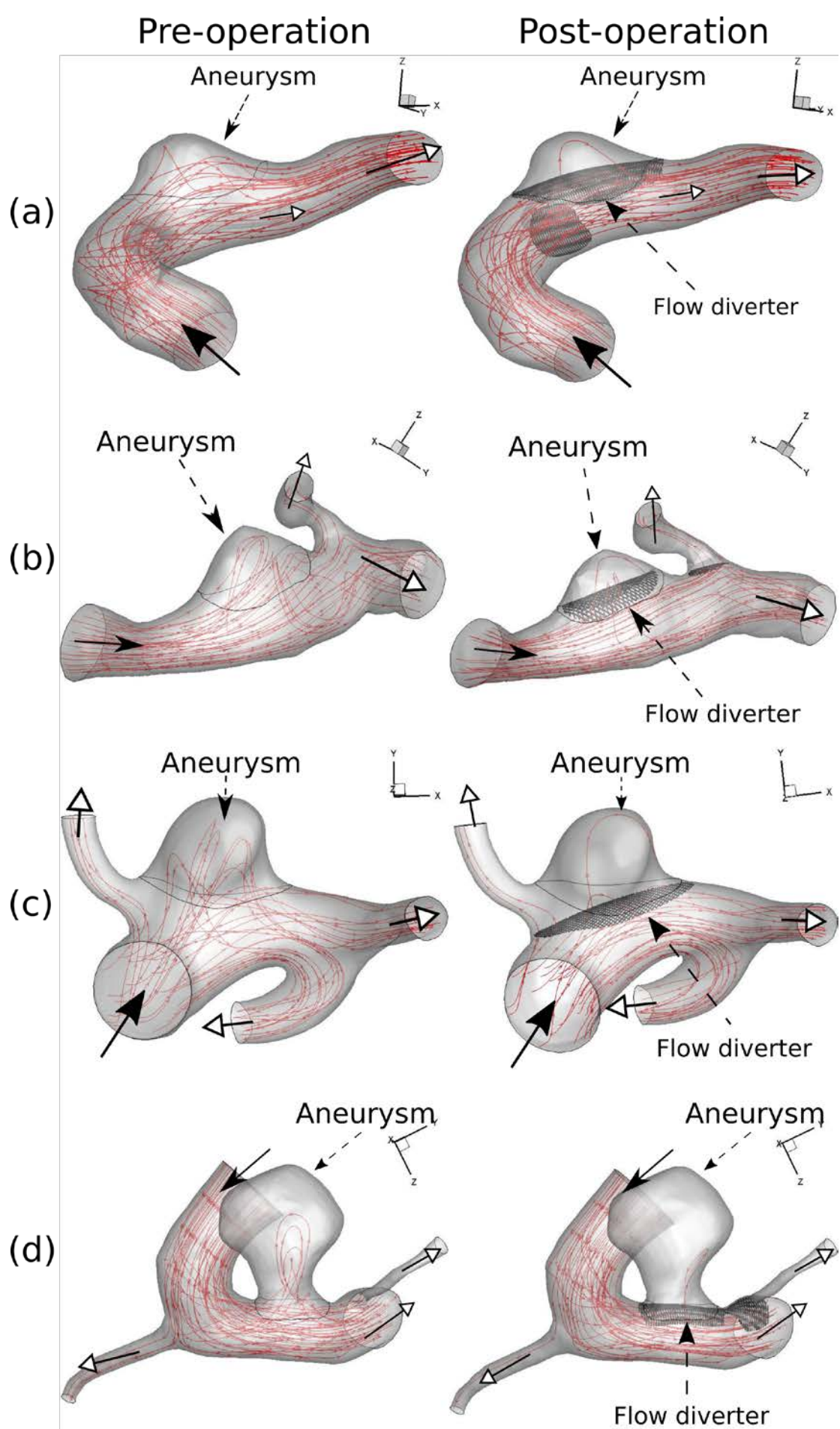


Fig8

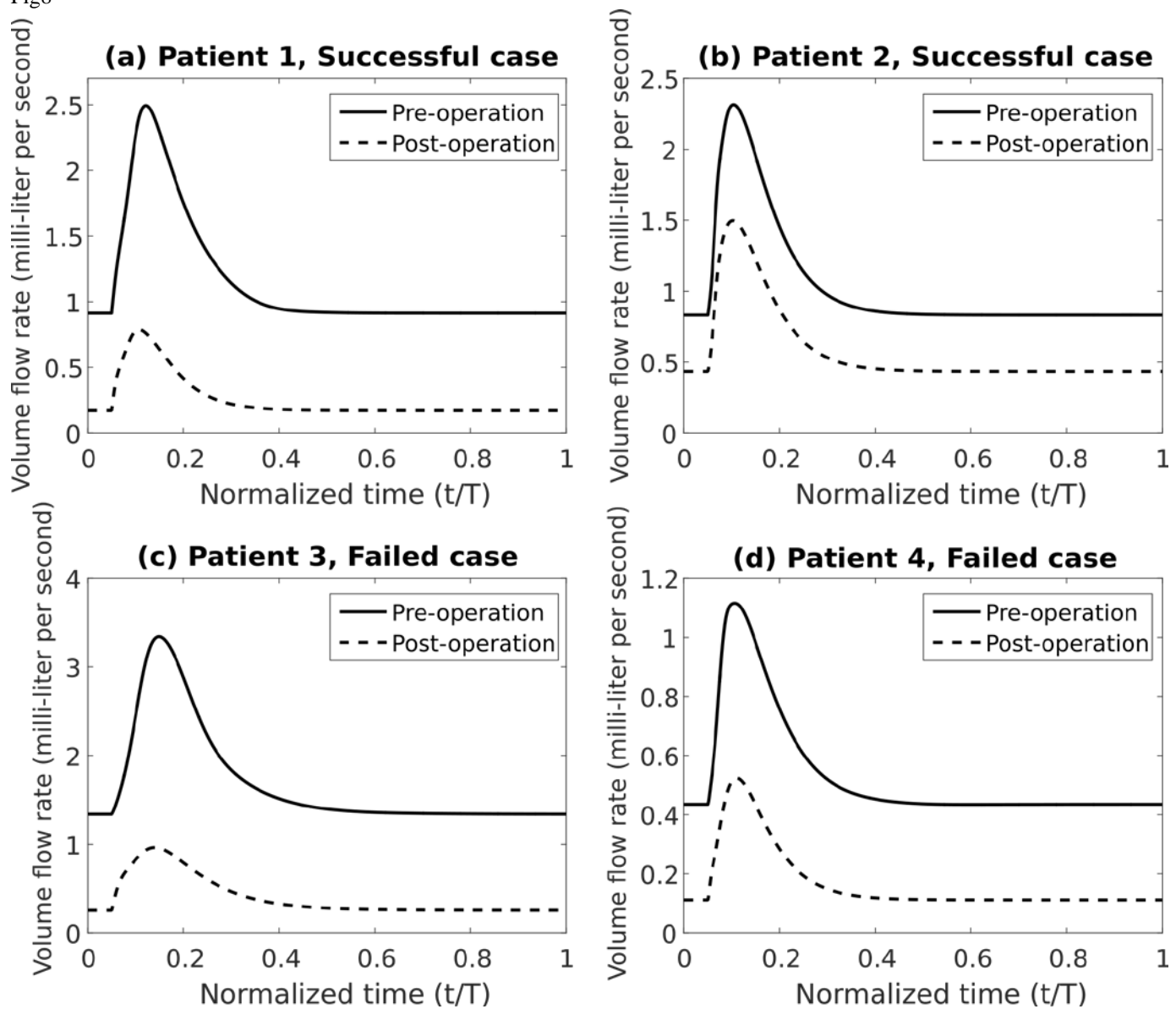


Fig9

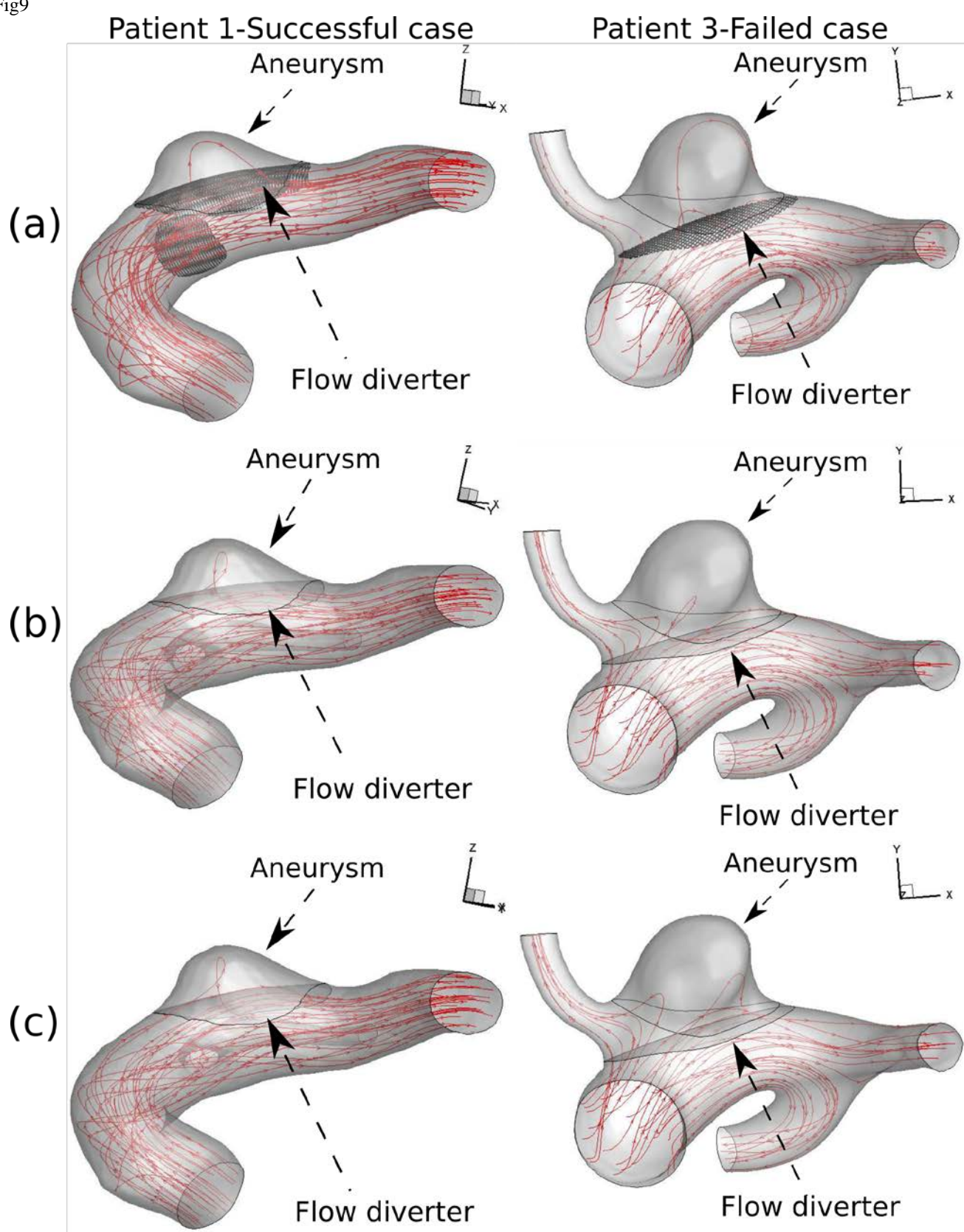


Fig10

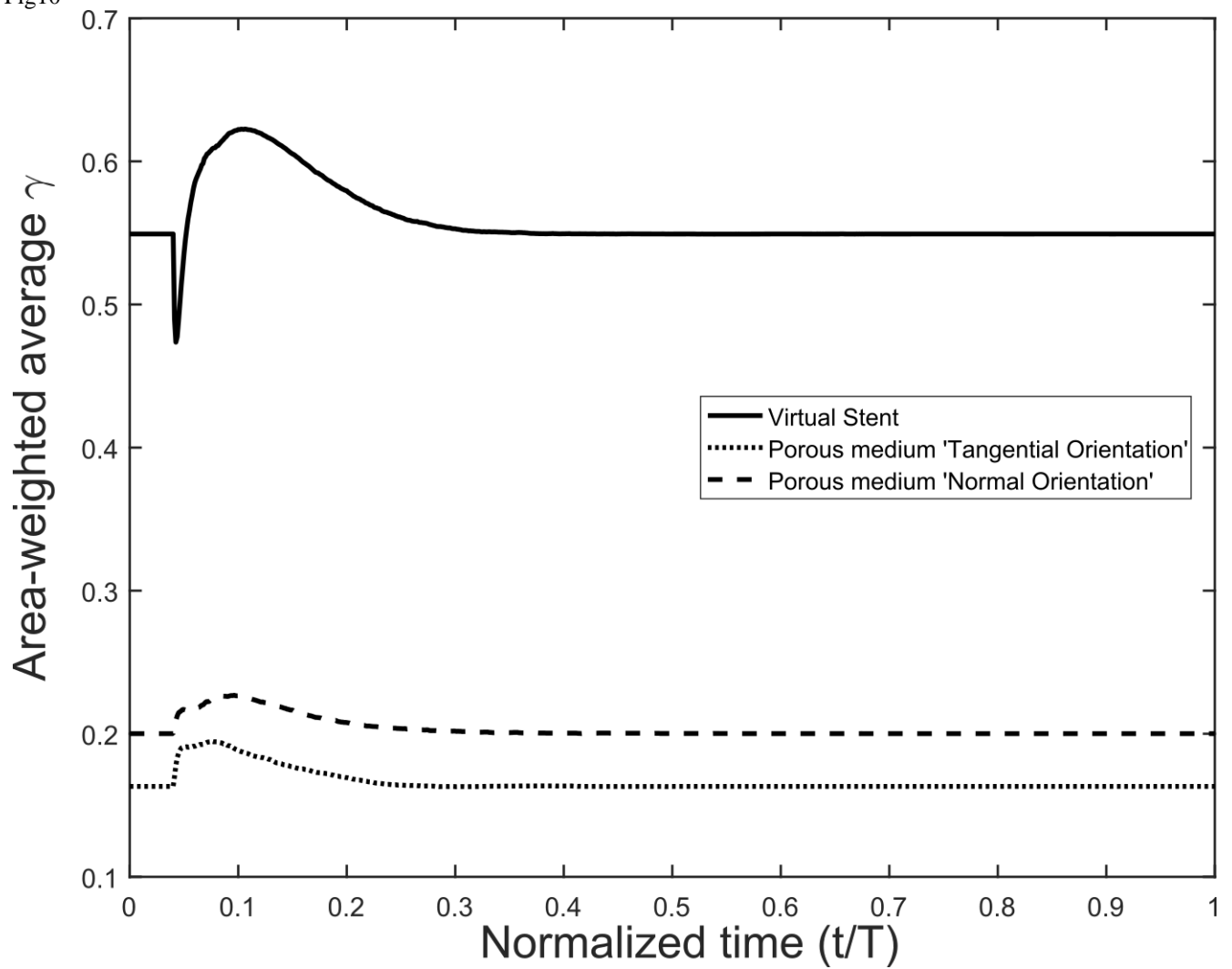


Fig11

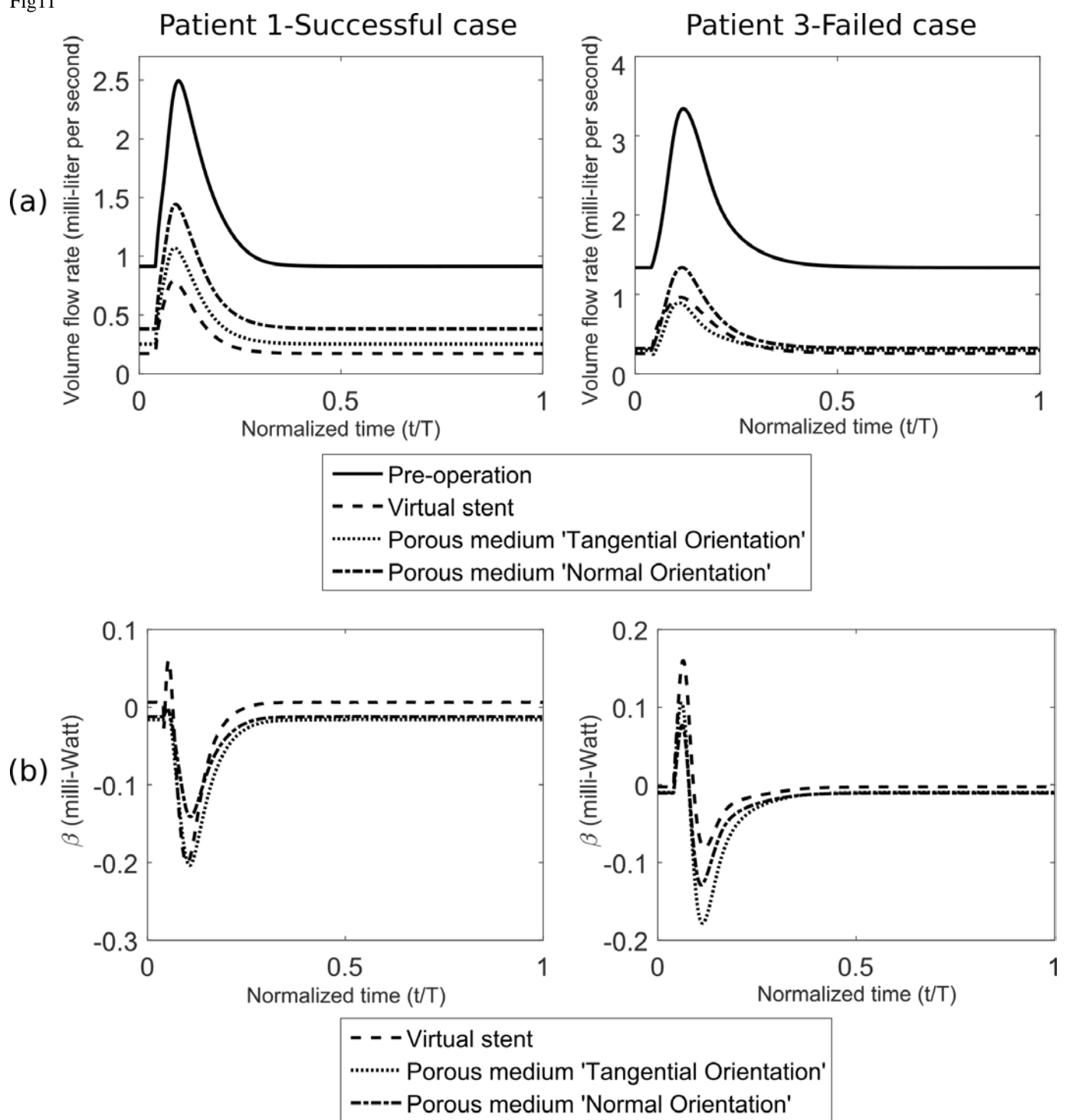


Fig12

